An Energy Harvesting Interface based on Reconfigurable Piezoelectric Harvester Array

Chen, Zhiyuan; Hao, Xianren; Li, Zhen; Ma, Yan; Wang, Jing; Liu, Xun; Du, Sijun; Han, Jun; Zeng, Xiaoyang

DOI
10.1109/TPEL.2025.3577696

Publication date
2025

Document Version
Final published version

Published in
IEEE Transactions on Power Electronics

An Energy Harvesting Interface Based on Reconfigurable Piezoelectric Harvester Array

Zhiyuan Chen, *Member, IEEE*, Xianren Hao, Zhen Li, Yan Ma, Jing Wang, Xun Liu, Sijun Du, *Senior Member, IEEE*, Jun Han, and Xiaoyang Zeng, *Senior Member, IEEE*

***Abstract*—This article presents a reconfigurable piezoelectric harvester array (RPA) designed for multi-input systems, which dynamically configures its structure based on the intensity of ambient vibrations. The proposed architecture enhances system efficiency by eliminating dc–dc converters and achieving maximum power point tracking through a single power stage. It also widens the input range by serially connecting PEH units, enabling operation at lower excitation levels. Additionally, this series connection reduces equivalent parasitic capacitance, improving flip efficiency and maximum output power improving rate (MOPIR).The proposed RPA is employed with classical parallel-synchronous switch harvesting on inductor technology and implemented using a 180 nm CMOS process. Experimental results demonstrate a conversion efficiency of up to 78%, an MOPIR of 5.93, and a minimum input voltage of 0.36 V. This highly integrated, wide-input-range, and energy-efficient scheme offers a novel approach to miniaturizing PEH systems. We present detailed design principles, operational mechanisms, and performance metrics, highlighting the RPA's potential as a scalable and environmentally friendly solution for powering next-generation Internet of Thing devices.**

***Index Terms*—DC–dc conversion, maximum power point tracking (MPPT), parallel-synchronous switch harvesting on inductor (P-SSHI), piezoelectric energy harvesting (PEH), reconfigurable piezoelectric harvester array (RPA).**

I. Introduction

With the advent of the Internet of Things (IoT) era, more sensor nodes are needed in nearly all fields such as manufacturing, healthcare, and security to achieve better interaction between humans and the environment. Piezoelectric energy harvesting (PEH) technology has been extensively researched as a solution to power the vast array of sensor nodes in modern systems. This technology leverages PEHs to convert environmental vibration energy into electrical energy. An interface circuit then processes this energy to meet the power requirements of the load.

The interface circuit in [1] achieves ac-dc conversion using a full bridge rectifier (FBR) and completes dc–dc conversion through a Buck type dc–dc converter. Maximum power point tracking (MPPT) is achieved with adaptive control technology. This traditional method for converting ac sources is known for its simplicity and stability. However, PEH is quite special compared to traditional ac sources. In its equivalent electrical model, in addition to the alternating current source i_P, there is also a parallel intrinsic capacitor C_P of nF level. The i_P repeatedly charges and discharges C_P due to phase changes in each cycle, causing energy loss. To address this issue, several optimization techniques for the ac–dc rectification stage have been proposed in academia, including synchronized switch harvesting on inductor (SSHI) [2], flipping capacitor rectifier [3], [4], and synchronized switch harvesting with capacitor and inductors [5].

Despite significant advancements in PEH interface circuit design, conventional PEH structures still face several critical challenges.

1) *Low Efficiency Due to Two-Stage Power Conversion:* Conventional structures typically employ a two-stage cascade design, necessitating dc–dc converters for MPPT. This additional power stage introduces significant conversion losses, reducing overall system efficiency. Even state-of-the-art dc–dc converters struggle to maintain high efficiency across a wide input range [6], further compromising system performance.
2) *Limited Input Range:* Conventional PEH systems require a minimum excitation level for startup and sustained operation [7], [8], [9]. The PEH open-circuit voltage must exceed a specific threshold, typically the forward voltage of the rectifier. This high minimum input voltage impedes system operation under low excitation intensities, often resulting in prolonged idle periods in practical applications where environmental vibration intensity fluctuates continuously.
3) *Low Flip Efficiency:* The conventional structure suffers from lower flip efficiency due to the presence of a high-value intrinsic capacitor in each PEH unit [10], [11], [12], [13]. This parasitic capacitance leads to charge waste during each half-cycle of vibration, significantly reducing the power extraction efficiency. Consequently, the system

Received 9 February 2025; revised 22 April 2025 and 21 May 2025; accepted 4 June 2025. Date of publication 9 June 2025; date of current version 5 August 2025. This work was supported by the Joint R&D Fund of Beijing Smart-chip Microelectronics Technology Co., Ltd. through Energy conversion chips supporting multiple energy harvesting scenarios under Grant SGSCDT00XPQT2400652. Recommended for publication by Associate Editor L. Corradini. *(Corresponding authors: Zhen Li; Jing Wang.)*

Zhiyuan Chen, Zhen Li, Jing Wang, Jun Han, and Xiaoyang Zeng are with the State Key Laboratory of Integrated Chips and Systems and School of Microelectronics, Fudan University, Shanghai 201203, China (e-mail: zhenli19@fudan.edu.cn; wangjing20@fudan.edu.cn).

Xianren Hao and Yan Ma are with Beijing Smart-chip Microelectronics Company Limited, Beijing 102200, China.

Xun Liu is with the School of Science and Engineering (SSE), Chinese University of Hong Kong, Shenzhen 518172, China.

Sijun Du is with the Department of Microelectronics, Delft University of Technology, 2628 CD Delft, The Netherlands.

Color versions of one or more figures in this article are available at https://doi.org/10.1109/TPEL.2025.3577696.

Digital Object Identifier 10.1109/TPEL.2025.3577696

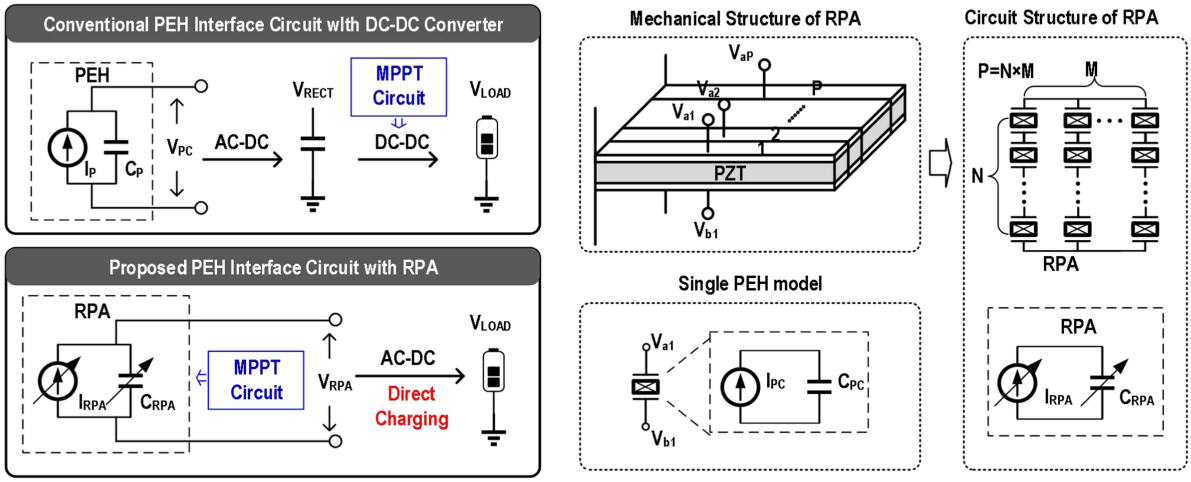

Fig. 1. Comparison of the conventional and the proposed RPA-based piezoelectric energy harvesting interface circuit.

experiences a lower maximum output power improving rate (MOPIR), limiting overall energy harvesting capability.

Appropriate series or parallel connections of different piezoelectric transducers (PTs) cannot only increase their bandwidth but also adjust the array's center frequency and equivalent impedance, thereby enhancing output power under varying application conditions. Given the performance advantages and design flexibility of multi-input arrays, numerous researchers have developed PEH interface systems based on PT arrays [14], [15], [16], [17]. Du and Seshia [14] adjusted the series-parallel relationship of two PT inputs based on vibration excitation intensity and voltage on storage capacitors, thereby improving the system's input voltage range and energy extraction efficiency. Du et al. [15] proposed the split-electrode synchronized-switch-harvesting-on-capacitors (SE-SSHC) technique to further optimize system performance. By dividing the PT electrode into four regions and connecting these regions in series when the piezoelectric current crosses zero to reduce the equivalent *Cp*, the system achieved a maximum output power ratio of 8.2 times (with off-chip diodes) and 5.2 times (with on-chip diodes) under low excitation levels. Meng [16] from the University of Pennsylvania developed a technology based on off-chip inductance sharing, simultaneously extracting energy from 6 PTs and achieving a maximum power ratio of 3.65x under impact vibration. In 2025, Fudan University proposed the cooperative flipping synchronous switched-capacitor (CF-SSHC) rectification technique [17]. Through cooperative work of multiple PT units, CF-SSHC can effectively increase the number of flipping phases, thereby achieving higher flipping efficiency and output power, enhancing PEH efficiency.

To address these issues, this article aims to implement a PEH interface circuit based on a reconfigurable piezoelectric harvester array (RPA). By adjusting the array configuration according to the excitation intensity, the use of a dc–dc converter can be avoided, improving the system's effective output power. At low excitation intensities, the open-circuit voltage of the RPA can be increased by connecting PEH units in series, allowing the system to collect energy at lower excitation intensities. Simultaneously, when PEH units are connected in series, the equivalent intrinsic capacitance of the RPA is reduced, increasing the MOPIR at low excitation intensities. This scheme provides a good solution for achieving energy self-sufficiency in wireless sensor systems in the IoT era.

The rest of this article is organized as follows: Section II introduces the operating mechanism of the proposed RPA-based system; Section III discusses the implementation of the system circuits. Section IV analyzes the test results. Finally, Section V concludes this article.

II. Proposed Piezoelectric Energy Harvester Based on RPA

A. Structure of the RPA

The comparison of the conventional and the proposed RPA-based PEH interface circuit is shown in Fig. 1. For conventional circuits, the ac voltage output by a single PEH is converted to dc voltage V_{RECT} through a ac–dc converter, which is then converted to the load voltage V_{LOAD} via a dc–dc converter. To extract maximum power from the PEH under different excitation levels, MPPT is typically required to adjust the voltage conversion ratio (VCR) of dc–dc converters. In conventional PEH, MPPT based on fractional open-circuit voltage (FOCV) operates on a fundamental principle: the maximum power point voltage (V_{MPP}) maintains a constant ratio to the open-circuit voltage (V_{OC}) across various vibration excitations. This relationship can be expressed mathematically as

$$V_{\mathrm{MPP}} = k \times V_{\mathrm{OC}} \tag{1}$$

where k is a constant coefficient, depending on the specific characteristics of the piezoelectric harvester. It is worth mentioning that adjusting the VCR of the dc–dc converter to achieve MPPT essentially involves adjusting the input impedance of the dc–dc converter. This adjustment enables the regulation of V_{RECT} (rectified voltage) to its optimal value (V_{MPP}) under different input excitations. The overall system efficiency (η_{System}) is the

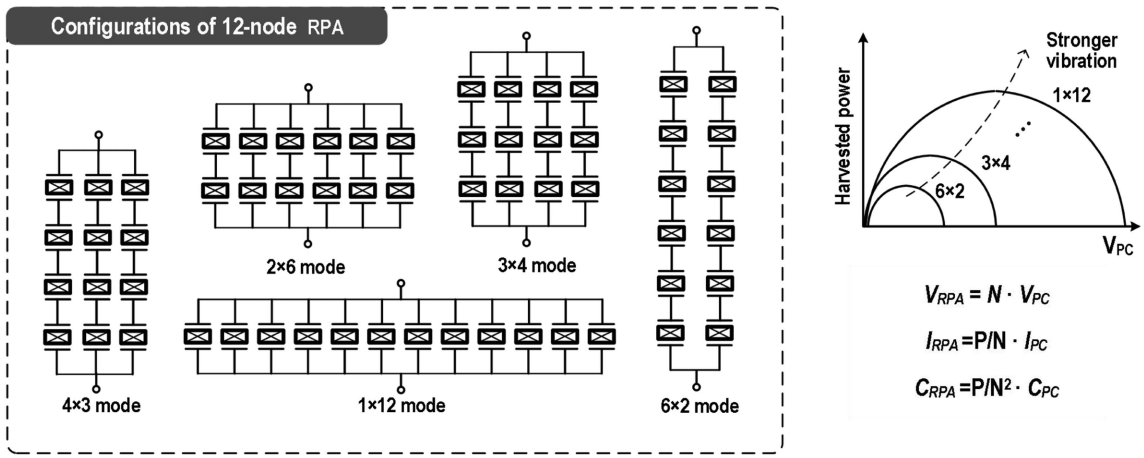

Fig. 2. Configuration of 12-node RPA under different vibration excitations.

product of the efficiencies of the ac–dc and dc–dc conversions. In the dc–dc converter, the power switches continuously switch between the on and off states under the control of the clock signal, and the switching losses ultimately reduce the system efficiency.

Therefore, we propose a RPA-based PEH interface circuit based on RPA. It achieves MPPT by adjust the configuration structure of the PEH without using a dc–dc converter. In the mechanical domain, we uniformly divide a whole PZT piece laterally, and assemble the upper and lower electrodes of the divided sections. Compared to a single PEH, the PEH units in the proposed RPA structure are closely arranged together. It indicates that all PEH units maintain similar states during vibration. In the electrical domain, each PEH can be equivalently modeled as a parallel connection of an ac current source $I_{\rm PC}$ and an intrinsic capacitor $C_{\rm PC}$. The PEHs are arranged in an N-row M-column RPA using power switches. Ignoring the parasitic capacitance and resistance of the power switches, the entire RPA can be equivalently modeled as an adjustable ac current source $I_{\rm RPA}$ in parallel with an adjustable capacitor $C_{\rm RPA}$. The electrical parameters of the RPA can be related to the electrical parameters of the PEH as follows:

$$V_{\rm RPA} = N \cdot V_{\rm PC} \tag{2}$$

$$I_{\rm RPA} = \frac{P}{N} \cdot I_{\rm PC} \tag{3}$$

$$C_{\rm RPA} = \frac{P}{N^2} \cdot C_{\rm PC} \tag{4}$$

where $V_{\rm RPA}$ is the open-circuit voltage of the RPA-based PEH interface circuit, and $V_{\rm PC}$ is the open-circuit voltage of a single PEH. Where P is the total number of PEH units in the RPA, N is the number of rows, and M is the number of columns in the RPA configuration. In our implementation, P = 12 with various configurations (N × M) including 1 × 12, 2 × 6, 3 × 4, 4 × 3, and 6 × 2. From (2), it can be seen that by adjusting the number of rows in the RPA, the equivalent output voltage of the RPA can be changed. The MPPT implementation for the RPA-based interface circuit system differs significantly from the traditional structure. The rectifier output voltage is directly fixed to the load voltage $V_{\rm LOAD}$. To achieve MPPT, it is necessary to satisfy

$$V_{\rm RPA} = k \cdot V_{\rm LOAD}. \tag{5}$$

Substituting (2) into (5) yields

$$N = \frac{k \cdot V_{\rm LOAD}}{V_{\rm PC}} \tag{6}$$

where $V_{\rm PC}$ exhibits a positive correlation with the external vibration level. Consequently, the RPA configuration (i.e., N) can be adjusted based on the level of external vibration, ensuring that the open-circuit voltage of the RPA satisfies the proportional relationship in (6), thereby achieving MPPT.

Fig. 2 illustrates the configuration of 12-node RPA under different vibration excitations. By configuring the switch array, the RPA can switch among five modes, ranging from 1 × 12 to 6 × 2. Under a fixed $V_{\rm LOAD}$, the number of rows N in the RPA decreases as the vibration excitation level increases. It is noteworthy that while alternative configurations exist for the 12-unit RPA, optimal performance is achieved only when the number of PT units is uniform across rows and columns. This uniformity allows all PT units to simultaneously reach their maximum power points. Uneven distribution of units among rows or columns would cause PT units to deviate from their optimal operating points, thereby reducing overall system efficiency.

The proposed RPA-based structure has the following advantages compared to the conventional structure.

1) *Enhanced System Efficiency:* In contrast to the conventional two-stage cascade structures, the proposed architecture eliminates the need for dc–dc converters. It efficiently achieves MPPT using a single power stage, thereby improving overall system efficiency.
2) *Wide Input Range:* Conventional PEH systems require a minimum excitation level for startup and sustained operation, necessitating that the PEH open-circuit voltage exceeds a specific threshold. The proposed architecture, however, achieves high RPA open-circuit voltage even at low excitation level by serially connecting all PEH units, thereby expanding the system's operational range.

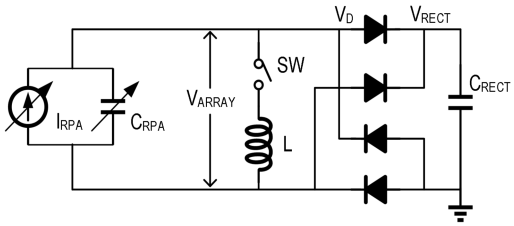

Fig. 3. Proposed piezoelectric energy harvesting system based on RPA and P-SSHI.

3) *High Flip Efficiency:* The proposed RPA-based structure reduces the equivalent parasitic capacitance when PEH units are connected in series, thereby enhancing the flip efficiency and MOPIR.

B. Performance Analysis of the RPA

Fig. 3 illustrates the proposed PEH system based on RPA and P-SSHI. In this configuration, V_{ARRAY} represents the voltage across the RPA, and V_D is the forward voltage drop across the diode in the rectifier. When the RPA delivers power to the load capacitor C_{RECT}, the rectifier's dc output voltage V_{RECT} satisfies the relationship: $V_{\mathrm{ARRAY}} = \pm(V_{\mathrm{RECT}} + 2V_D)$. As I_{RPA} crosses zero, switch SW conducts, forming an *LC* circuit with C_{RPA} and inductor L, which quickly flips the voltage polarity across the RPA. Due to nonideal factors such as parasitic resistance, an equivalent resistance R_{BF} exists in the *LC* circuit. This resistance causes damping losses after the polarity flip, calculated as

$$V_{FS} = (V_{\mathrm{RECT}} + 2V_D) \cdot \varphi_{(N)} \tag{7}$$

where

$$\begin{aligned}\varphi_{(N)} &= 1 - e^{\beta_{(N)}}, \beta_{(N)} \\ &= -\pi \cdot R_{\mathrm{BF}} \sqrt{\frac{PC_{\mathrm{PC}}}{4 \cdot N^2 \cdot L - P \cdot R_{\mathrm{BF}}^2 \cdot C_{\mathrm{PC}}}}\end{aligned} \tag{8}$$

where $\varphi(N)$ represents the voltage flipping efficiency which varies with different RPA configurations. R_{BF} is the parasitic resistance (Ω) of the inductor L, N represents the number of piezoelectric elements connected in parallel within each series-connected group, and L is the inductance (H) of the SSHI circuit. P is the total number of piezoelectric elements in the array, and C_{PC} is the individual capacitance (F) of each piezoelectric element.

Based on this model and assumptions, the vibration period of the PEH is denoted as T, and the charge generated by the RPA every half cycle is

$$Q_{\mathrm{total-RPA}} = \int_0^{\frac{T}{2}} I_{\mathrm{RPA}} \cdot \sin\, \omega t\, dt = 2C_{\mathrm{RPA}} V_{\mathrm{RPA}}. \tag{9}$$

The charge extracted by the P-SSHI rectifier from the RPA every half cycle is

$$\begin{aligned}Q_{\mathrm{SSHI-RPA}} &= Q_{\mathrm{total-RPA}} - V_{\mathrm{FS}} C_{\mathrm{RPA}} \\ &= C_{\mathrm{RPA}} \left[2V_{\mathrm{RPA}} - (V_{\mathrm{RECT}} + 2V_D) \cdot \varphi\right].\end{aligned} \tag{10}$$

Consequently, the energy harvested by the P-SSHI rectifier in each half-cycle is expressed as

$$\begin{aligned}E_{\mathrm{SSHI-RPA}} &= V_{\mathrm{RECT}} \cdot Q_{\mathrm{SSHI-RPA}} \\ &= V_{\mathrm{RECT}} C_{\mathrm{RPA}} \left[2V_{\mathrm{RPA}} - (V_{\mathrm{RECT}} + 2V_D) \cdot \varphi\right].\end{aligned} \tag{11}$$

Finally, the output power of the proposed SSHI-RPA system is derived as

$$\begin{aligned}P_{\mathrm{SSHI-RPA}} &= 2fV_{\mathrm{RECT}} C_{\mathrm{RPA}} \left[2V_{\mathrm{RPA}} - (V_{\mathrm{RECT}} + 2V_D) \cdot \varphi\right] \\ &= 2\frac{P}{N^2} fV_{\mathrm{RECT}} C_{\mathrm{PC}} \left[2NV_{\mathrm{PC}} - (V_{\mathrm{RECT}} + 2V_D) \cdot \varphi\right]\end{aligned} \tag{12}$$

where $f = 1/T$.

Subsequently, by deriving the outpower with respect to V_{RECT}, the optimal $V_{\mathrm{RECT,OPT}}$ is determined where the derivative equals zero

$$\frac{dP_{\mathrm{SSHI-RPA}}}{dV_{\mathrm{RECT}}} = 4fC_{\mathrm{RPA}} \left[V_{\mathrm{RPA}} - \varphi V_D - \varphi V_{\mathrm{RECT}}\right] \tag{13}$$

$$\frac{dP_{\mathrm{SSHI-RPA}}}{dV_{\mathrm{RECT}}} = 0 \xrightarrow{\text{yields}} V_{\mathrm{RPA}} = \varphi \cdot (V_{\mathrm{RECT}} + V_D) \tag{14}$$

$$V_{\mathrm{RECT,OPT}} = \frac{V_{\mathrm{RPA}} - \varphi \cdot V_D}{\varphi} = \frac{N \cdot V_{\mathrm{PC}} - \varphi \cdot V_D}{\varphi}. \tag{15}$$

The maximum output power is then given by

$$\begin{aligned}P_{\mathrm{SSHI-RPA,MAX}} &= 2\frac{P}{N^2} fV_{\mathrm{RECT,OPT}} C_{\mathrm{PC}} \\ &\left[2NV_{\mathrm{PC}} - (V_{\mathrm{RECT,OPT}} + 2V_D) \cdot \varphi\right].\end{aligned} \tag{16}$$

To evaluate the ratio of actual output power to theoretical maximum output power for the proposed RPA-SSHI system, we define the efficiency of the SSHI-RPA system as follows:

$$\text{Efficiency} = \frac{P_{\mathrm{SSHI-RPA}}}{P_{\mathrm{SSHI-RPA,MAX}}}. \tag{17}$$

This efficiency metric quantifies how closely the system's performance approaches its theoretical maximum. An efficiency value of 1 indicates that the system is operating at its theoretical maximum power output. Values below 1 suggest room for performance improvement.

C. MPPT Scheme Based on RPA

Fig. 4 illustrates the relationship between output power and open-circuit voltage of a 12-node RPA under different combinations. It shows that the output power is proportional to the open-circuit voltage for all 12-node RPA configurations. For lower open-circuit voltages (V_{PC}), higher output power is achieved by connecting more PEH units in series within the RPA ($N = 12$); whereas, with larger V_{PC} values, the PEH units in the RPA are primarily connected in parallel. Adjusting the combination of RPA can be equivalent to adjusting the open-circuit voltage of the RPA; therefore, under a given V_{PC}, selecting the optimal N based on the value of V_{PC} can achieve MPPT.

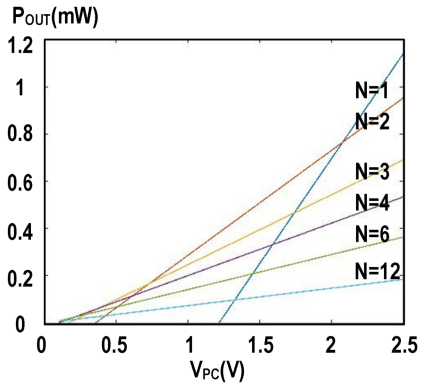

Fig. 4. Relationship between output power and open-circuit voltage of 12-node RPA under different combinations.

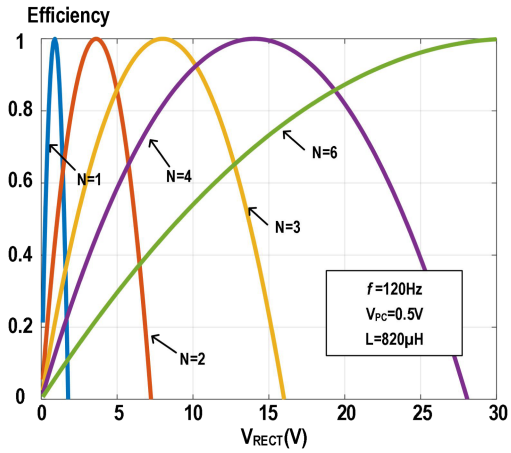

Fig. 5. Efficiency of RPA-based system versus rectifier voltage (V_{RECT}) under different combinations.

Fig. 5 illustrates the efficiency of RPA-based system versus rectifier voltage (V_{RECT}) under different combinations. A traditional single PEH can be equivalent to the RPA configuration at $N = 1$, achieving MPPT by adjusting V_{RECT}. The figure indicates that at $N = 1, 2, 3, 4, 6$, the optimal $V_{\mathrm{RECT,OPT}}$ are 1, 2.5, 7, 12, 25 respectively. However, when $N = 12$, $V_{\mathrm{RECT,OPT}}$ exceeds 30V, far surpassing practical application scenarios. The optimal $V_{\mathrm{RECT,OPT}}$ increases with increasing N.

Fig. 6 illustrates the calculated efficiency versus input excitation (V_{PC}) when V_{RECT} is set at 4.2 V. It is evident that if the system adjusts the RPA configuration based on V_{PC}, it can harvest energy within a V_{PC} range of 2–6.5 V while maintaining an efficiency of over 68%. Theoretically, the maximum efficiency can reach 100%, and this efficiency will not be further reduced by the introduction of a dc–dc converter. Although traditional schemes can also achieve a theoretical efficiency of 100%, the inclusion of a subsequent dc–dc converter will significantly reduce the maximum efficiency of the entire system.

III. Circuit Implementations

Fig. 7 shows the schematic diagram of the proposed system. The entire interface circuit is composed of four primary modules: the power switch array, the P-SSHI active rectifier,

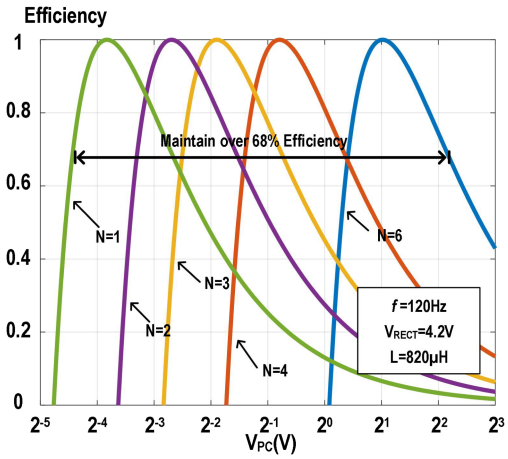

Fig. 6. Theoretical calculation of efficiency versus input excitation (V_{PC}) for different 12-node RPA configurations.

the Biasflip controller, and the MPPT module. The RPA is formed by twelve PEH units and the power switch array. RPA's AC output is rectified through P-SSHI circuitry, functioning either in V_{load} mode (powering devices directly) or V_{bat} mode (efficiently charging a 3.7–4.2V battery with optimized current). Upon changes in excitation strength, the MPPT module activates and it then adjusts the switch array configuration based on the V_{OC} value. The Biasflip controller manages the on-off state of the *LC* flipping loop, activating the power switch via $V_{G1/2}$ output when iRPA crosses zero. Due to variations in the inherent capacitance (C_{RPA}) of the RPA under different configurations, the *LC* resonance period fluctuates. To address this, on-chip Schottky diodes are employed to achieve passive adaptive turn-OFF of the *LC* circuit. In the following sections, we will sequentially present the circuit structure of each module.

A. Power Switch Array

Fig. 8 illustrates the structure of the power switch. Each power switch comprises parallel-connected PMOS and NMOS transistors, with the substrate of the power transistor using active body biasing technology. RPA switching occurs in hundreds of nanoseconds through 3600 μm/0.5 μm MOSFETs, significantly faster than piezoelectric vibration periods. The system dynamically reconfigures during operation without interrupting energy harvesting, enabling efficient adaptation across various environmental conditions. To optimize area efficiency, the power switch array is designed hierarchically. Specifically, two PEH units and three power switches form a cell 2 unit. When the control signal V_{SEL0} is high, the two PEH units are connected in parallel; otherwise, they are connected in series. Following a similar structure, two cell 2 units form a cell 4 unit, and three cell 4 constitute the RPA. The whole RPA employs 33 power switches and 10 inverters. Notably, despite incorporating 33 power switches and 10 inverters in the design, the power switch array has minimal impact on harvester efficiency, consuming only 5.2 nW of static power, which accounts for merely 0.3% of the total power consumption. The table in Fig. 8 delineates

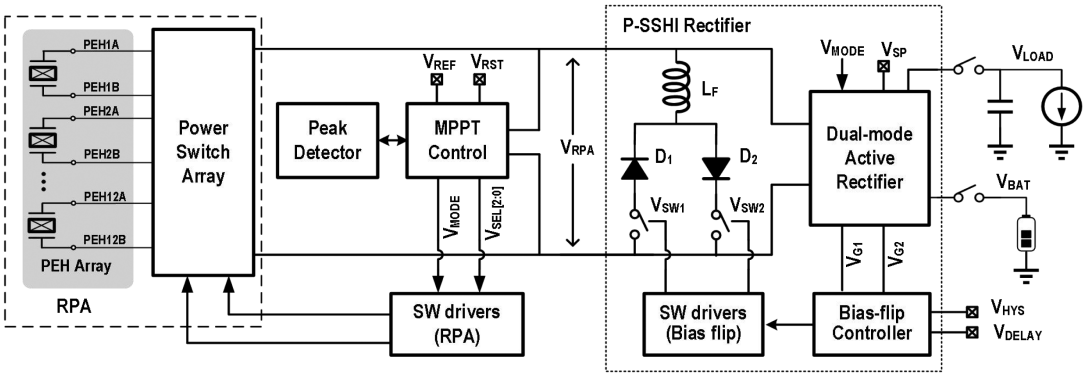

Fig. 7. Block diagram of the proposed piezoelectric energy harvesting system.

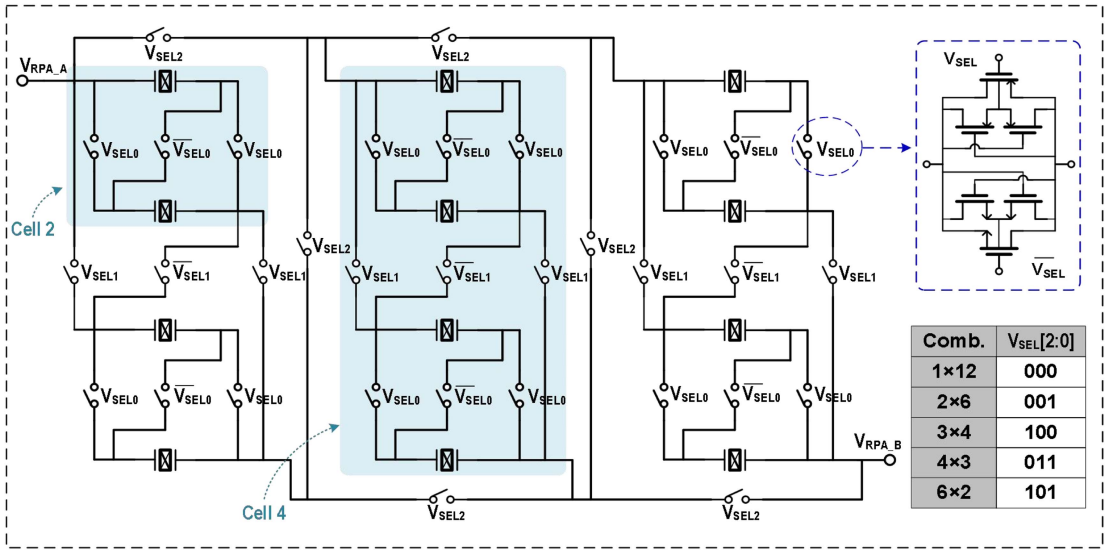

Fig. 8. Structure of the power switch array.

the relationship between $V_{\mathrm{SEL}[2:0]}$ and the corresponding RPA configurations.

B. Dual-Mode Active Rectifier

The active rectifier employed in the proposed system is depicted in Fig. 9. As the proposed system dynamically adjusts the RPA configuration based on excitation strength, I_{RPA} varies over a wide range from μA to mA. This wide current range poses challenges in dimensioning the four MOS transistors. If a high *W/L* ratio is employed, comparators require stronger driving capabilities; otherwise, signal delays due to load capacitance would result in energy losses. Moreover, when small currents pass through large-sized power transistors, the resulting voltage drop becomes too small, potentially causing anomalous comparator detection [18], [19], [20]. Conversely, if MOS transistors with low *W/L* ratios are used, the forward voltage drop V_D of the active diodes increases under high I_{RPA} conditions, which would similarly reduce the power collection efficiency of the system. To address this, a dual-mode active rectifier is implemented, featuring a main path and an auxiliary path. In Fig. 9, the

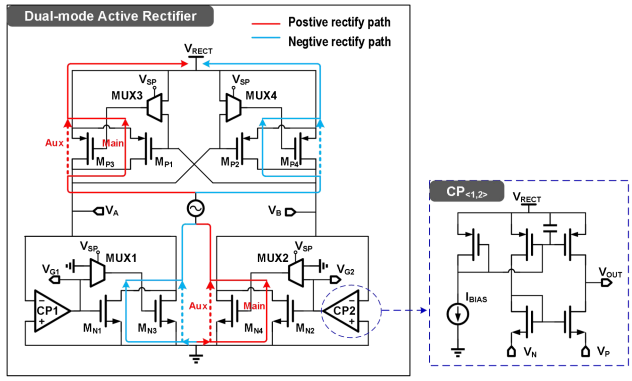

Fig. 9. Dual-mode active rectifier.

smaller M_{P1}, M_{P2}, M_{N1}, and M_{N2} function as the main switch transistors in the primary path, while the larger M_{P3}, M_{P4}, M_{N3}, and M_{N4} act as auxiliary switch transistors in the secondary path. The primary path is continually active, but the auxiliary path is activated by the V_{SP} control signal only under conditions of high excitation strength. The V_{SP} signal is derived by encoding

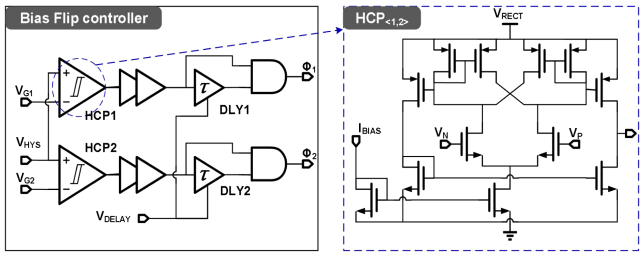

Fig. 10. Bias Flip Controller.

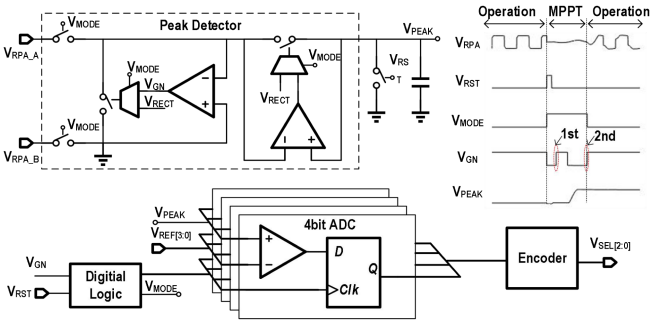

Fig. 11. MPPT control module.

the array's control signals, $V_{\mathrm{SEL}[2:0]}$. The system can self-start without V_{rect} precharging through the parasitic full-bridge rectifier formed by MOSFET body diodes in the active rectifier. These diodes initially function as a passive bridge for startup charging, before transitioning to efficient active rectification once sufficient voltage is reached.

C. Bias Flip Controller

To minimize chip area and system power consumption, the zero-crossing detection functionality is implemented by the comparators within the active rectifier. Assuming $I_{\mathrm{RPA}} > 0$, V_{G1} is high, and V_{G2} is low, M_{N1} and M_{P2} are conducting, while M_{N2} and M_{P1} are cut OFF, rectifying V_{RPA}. When I_{RPA} crosses zero, the output signals $V_{G1/2}$ from $C_{P1/2}$ switch from high to low, turning off the NMOS transistors, with $V_{G1/2}$ also serving as the input signals for the flipping control module. Fig. 10 illustrates the bias-flip controller. The hysteresis comparators, serving as the input module for the bias flip controller, is used to filter out any jitter that might occur at the zero-crossing point, and together with two subsequent inverters, it is utilized to detect the falling edge of $V_{G1/2}$. The delay unit, inverter, and AND gate in the bias flip controller then form a single pulse generator.

D. MPPT Controller

The MPPT controller, illustrated in Fig. 11, produces the signal V_{SEL} based on the open-circuit voltage V_{OC} to optimally configure the combination of the RPA. Our system employs an FOCV-based MPPT approach that performs a complete scan during startup or restart to determine optimal RPA configuration. This design choice is based on power consumption and stability considerations. Continuous MPPT execution would consume additional energy, which is unnecessary when vibration conditions remain relatively stable. The MPPT controller consists of four main components: a peak detection circuit, a 4-bit ADC, a digital control unit, and an encoder. When the reset signal V_{RST} generates a high-level pulse, it triggers the system's mode indication signal V_{MODE}, switching from the operational state to the MPPT state. In this mode, the active rectifier is deactivated while the RPA array is configured to a 1x12 mode, and the peak voltage in the peak detector is reset to zero.

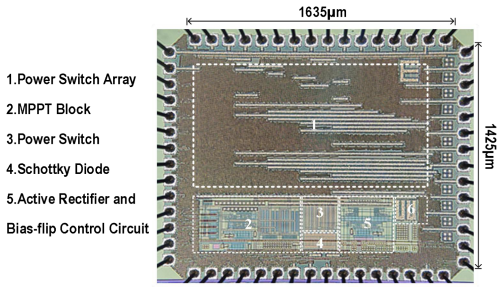

Fig. 12. Chip photograph.

During MPPT operation, whenever the peak detector identifies the peak voltage of V_{RPA}, V_{GN} produces a rising edge signal. To prevent false detection when the V_{RST} pulse occurs during the positive half-cycle of V_{RPA}, the detected value is only fed into the 4-bit ADC for comparison with the reference voltage after V_{GN} has appeared twice. V_{GN} is a pulse signal generated by the peak detection circuit when detecting V_{RPA} peaks, and the system requires two V_{GN} pulses to confirm a true detection, preventing peak detection errors when V_{RST} occurs during the positive half-cycle of V_{RPA} and ensuring complete cycle observation. The result of this comparison is then encoded into $V_{\mathrm{SEL}[2:0]}$ to ensure the optimal configuration of the RPA mode. Subsequently, V_{MODE} transitions from high to low, signaling the completion of the MPPT cycle.

IV. Measurement Results

The proposed circuit is fabricated using a 180 nm CMOS process and occupies a chip area of 2.33 mm^2. The chip photograph is depicted in Fig. 12. For testing, we employ custom PEHs, each measuring 3 mm by 45 mm, with an inherent capacitance of approximately 15 nF per PEH. To ensure that all 12 PEH units exhibit roughly the same amplitude and phase, they are mounted together on a fixture and affixed to the same vibrating end. In our experimental setup, a Keithley 2614B source meter connected to the V_{load} port served as the system load, operating in voltage source mode to simulate different load conditions while simultaneously measuring current to calculate output power at each operating point.

Fig. 13 shows measured waveforms during MPPT, demonstrating the transition from 1 × 12 mode to 3 × 4 mode. The mode switching of the RPA is a controlled and responsive process managed by the MPPT controller. It follows a defined state machine sequence, with transitions governed by deliberate control logic rather than sudden or unstable behavior. Initially, with $V_{\mathrm{OC}} = 3$ V, the RPA operates in a 1 × 12 mode for

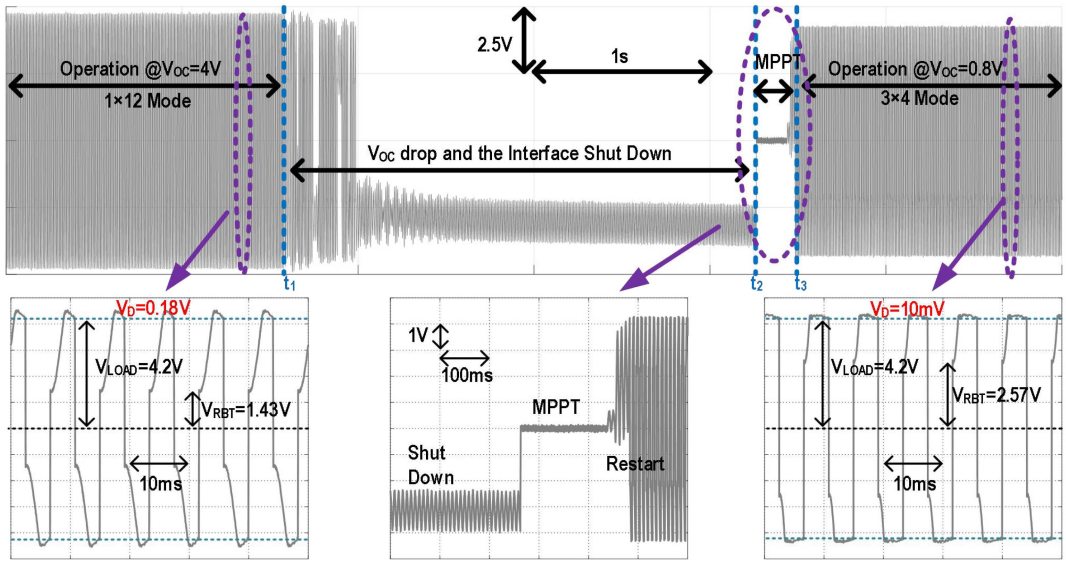

Fig. 13. Measured waveforms during MPPT.

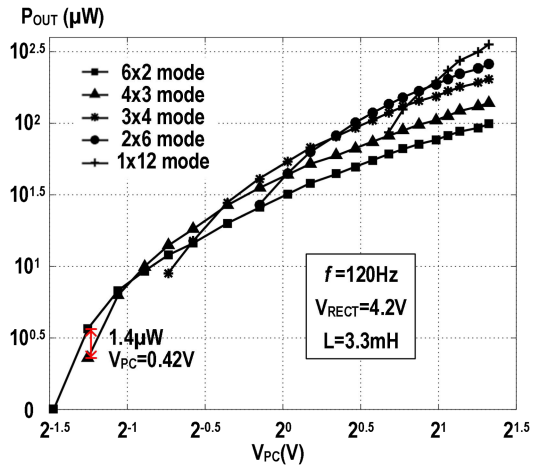

Fig. 14. Measured output power (P_{OUT}) versus open-circuit voltage (V_{PC}) under different configurations.

energy harvesting. In this configuration, the auxiliary switches are disabled, and the forward voltage V_D across the active diodes is approximately 180 mV. At time t_1, V_{OC} decreases to 0.8 V, causing the PEH circuit to cease effective energy harvesting. At moment t_2, the MPPT function is activated, and following a brief reconfiguration, the RPA is adjusted to a 3 × 4 mode, allowing the system to resume effective energy harvesting operations. Notably, in this 3 × 4 mode, V_D is reduced to about 10 mV, primarily due to the change in current flowing through the rectifier. The switching occurs during a clearly defined MPPT operation phase (between t 2 and t 3) and is triggered after VOC decreases. During transition, the rebuilt voltage VRBT increases from 1.43 to 2.57 V due to C_{RPA} reduction. These results align well with theoretical predictions. The switching mechanism is managed by the MPPT controller, which generates the V_{SEL} signal based on V_{OC} to optimize RPA configuration.

Fig. 14 illustrates the measured output power (P_{OUT}) versus open-circuit voltage (V_{PC}) under different configurations. It can be observed that at lower V_{PC} values, the system outputs higher power when the PEH units are connected in series. Correspondingly, at higher V_{PC} values, parallel connection of PEH units yields higher output power. At $V_{\mathrm{PC}} = 0.42$ V, the output power in the 6 × 2 mode is 1.4 μW higher than in the 4 × 3 mode, representing a 60% increase. Additionally, in the 1 × 12 mode (which can be equated to a traditional single PEH structure), the system only begins to operate and harvest energy when V_{PC} exceeds 1.6 V, whereas in the 6 × 2 mode, it can effectively harvest 1 μW of power at just $V_{\mathrm{PC}} = 0.36$ V. Therefore, the proposed interface circuit effectively broadens the system's input range. Since the proposed system can achieve optimal RPA configuration based on environmental excitation without requiring additional dc–dc conversion, at any specific open-circuit voltage and fixed load voltage ($\mathrm{V_{LOAD}}$), there exists an optimal combination of $\mathrm{V_{PC}}$ and RPA configuration that enables the system to operate very close to the maximum power point, achieving up to 99% MPPT efficiency.

Fig. 15 shows the relationship between the system's flip efficiency and V_{LOAD}. When V_{LOAD} is lower, the flipping loss is greater due to higher resistance in the switch array; however, as V_{LOAD} increases, flip efficiency significantly improves. Simultaneously, although passive shutoff of the *LC* circuit using diodes results in some flipping loss due to the forward voltage drop across the diodes, the system still achieves notable flip efficiency.

Although the proposed MPPT mode differs from traditional configurations, MOPIR tests were still conducted for a better performance comparison. Under fixed excitation strength, different RPA arrangements result in varying optimal V_{LOAD}, which may exceed the normal operating range of the chip under some test conditions. Consequently, for convenience in testing, the RPA was set to a 2 × 6 mode. As shown in Fig. 16, when V_{PC} is fixed at 1V, the proposed circuit outputs a maximum power

TABLE I
COMPARISON OF THE PERFORMANCE

	This article	[2]	[4]	[7]	[14]	[8]
Technology	**0.18um**	0.35um	0.18um	0.18um	0.18um	65nm
Technique	**P-SSHI**	P-SSHI	SPFCR	P-SSHI	SE-SSHC	SECE
Key Component	**Inductor**	Inductor	Four Capacitors	Inductor	Eight Capacitor	Inductor
P_{in} Adaptation	**Reconfigurable PEH Array**	Inductive dc – dc	SC dc – dc	Trickle Charger	N/A	MSVR
No. of Inputs	**12**	1	1	1	4	3
Piezoelectric Capacitor	**180nF (15nF each)**	12nF	22nF	8.5nF	1.94nF	N/A
MOPIR	**5.93x**	4x	9.3x	2.48x	5.2x	3.2x
Operating Freq.	**120Hz**	225 Hz	200 Hz	155 Hz & 419 Hz	219 Hz	N/A
Chip Size	**2.33 mm^2**	4.25 mm^2	0.2 mm^2	0.3 mm^2	5.3 mm^2	3.11 mm^2
Max. Voltage Flipping Eff.	**0.78**	0.75	0.84	0.75	0.69	N/A
Max. MPPT Efficiency	**99%**	85%	92%	>89%	N/A	80% (Overall)

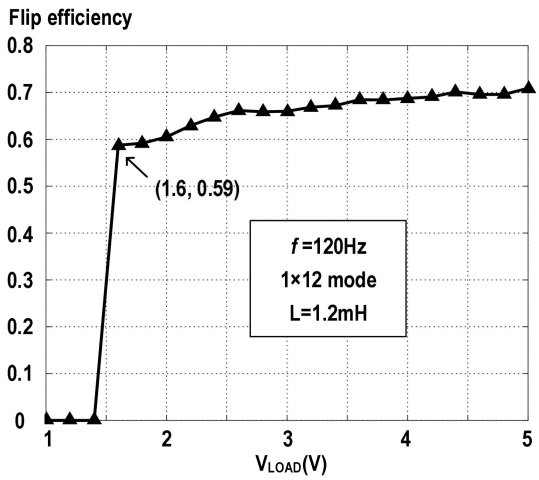

Fig. 15. Relationship between the flip efficiency and V_{LOAD}.

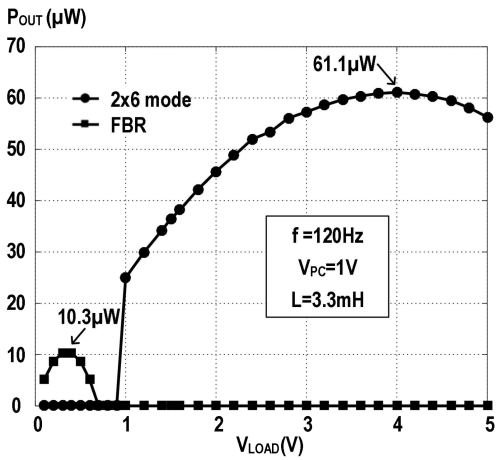

Fig. 16. Measured output power (P_{OUT}) versus load voltage (V_{LOAD}).

of 61.1 μW, compared to the theoretical maximum of 10.3 μW for the FBR, where V_D is set at 0.15 V. Hence, the MOPIR can reach 5.93x.

Fig. 17 shows the corresponding test results for the proposed dual-mode active rectifier. To reduce V_D in the 1 $\times$ 12 mode, the incorporation of auxiliary switches significantly enhances energy harvesting when the RPA is configured in 1 $\times$ 12 mode. For example, when $V_{\mathrm{OC}} = 1.28$ V, the auxiliary path contributes to a 15% increase in the system's output power. Conversely, in the 6 $\times$ 2 mode, operating solely with the main path is more effective for energy collection.

Table I compares the performance of the proposed PEH system with state-of-the-art systems. Our design features an

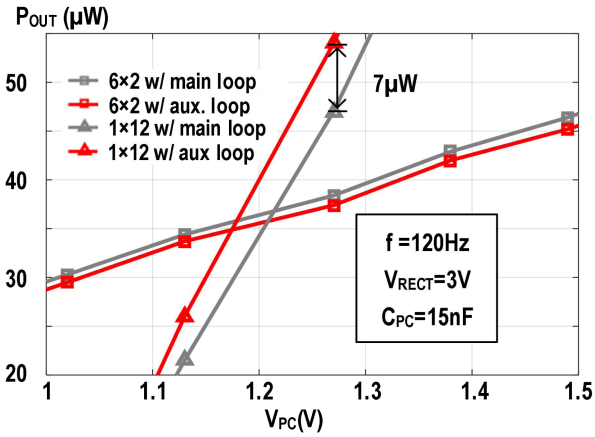

Fig. 17. Test results for the proposed dual-mode active rectifier.

RPA array comprising 12 PEH units, facilitating multi-input energy harvesting. Through the serial connection of PEH units within the array and the application of P-SSHI technology, our design achieves a maximum MOPIR of 5.93 times. Despite the incorporation of Schottky diodes in the *LC* circuit leading to some energy loss, the flipping ratio remains high at 0.78. Our design innovatively modifies the RPA structure to implement MPPT, thereby avoiding the switching losses typically associated with dc–dc converters and achieving an MPPT efficiency of up to 99%. The system comprehensively implements the requisite ac–dc conversion, voltage transformation, and MPPT functionalities essential for PEH, providing an effective solution for energy self-sufficiency in sensor nodes during the Internet of Things era.

V. Conclusion

This article presents a novel PEH scheme combining an RPA with P-SSHI rectification technology. The proposed scheme achieves dc–dc conversion functionality without introducing additional passive devices and can adjust the RPA configuration based on excitation intensity to realize MPPT. Furthermore, it expands the input range and improves flipping efficiency through serial connection of PEH units. Experimental results demonstrate a reduced minimum input voltage of 0.36 V, a conversion efficiency of up to 78%, and a maximum MOPIR of 5.93.

References

[1] G. K. Ottman, H. F. Hofmann, A. C. Bhatt, and G. A. Lesieutre, "Adaptive piezoelectric energy harvesting circuit for wireless remote power supply," *IEEE Trans. Power Electron.*, vol. 17, no. 5, pp. 669–676, Sep. 2002.

[2] Y. K. Ramadass and A. P. Chandrakasan, "An efffcient piezoelectric energy-harvesting interface circuit using a bias-FFIP rectiffer and shared inductor," in *Proc. IEEE Int. Solid-State Circuits Conf. - Dig. Tech. Papers*, 2009, pp. 296–297.

[3] Z. Chen, M.-K. Law, P.-I. Mak, W. H. Ki, and R. P. Martins, "22.2 A 1.7mm2 inductorless fully integrated flipping-capacitor rectifier (FCR) for piezoelectric energy harvesting with 483 power-extraction enhancement," in *Proc. IEEE Int. Solid-State Circuits Conf.*, 2017, pp. 372–373.

[4] Z. Chen, M.-K. Law, P.-I. Mak, X. Zeng, and R. P. Martins, "Piezoelectric energy-harvesting interface using split-phase flipping-capacitor rectifier with capacitor reuse for input power adaptation," *IEEE J. Solid-State Circuits*, vol. 55, no. 8, pp. 2106–2117, Aug. 2020.

[5] B. Ciftci, S. Chamanian, A. Koyuncuoglu, A. Muhtaroglu, and H. Kulah, "A low-profile autonomous interface circuit for piezoelectric micro-power generators," *IEEE Trans. Circuits Syst. I, Reg. Papers*, vol. 68, no. 4, pp. 1458–1471, Apr. 2021.

[6] Z. Xia and J. Stauth, "17.1 A two-stage cascaded hybrid switched-capacitor DC-DC converter with 96.90.6V/s input slew rate during startup," in *Proc. IEEE Int. Solid-State Circuits Conf.*, 2021, vol. 64, pp. 256–258.

[7] E. E. Aktakka and K. Najaff, "A micro inertial energy harvesting platform with self-supplied power management circuit for autonomous wireless sensor nodes," *IEEE J. Solid-State Circuits*, vol. 49, no. 9, pp. 2017–2029, Sep. 2014.

[8] S. Li, X. Liu, and B. H. Calhoun, "A 32nA fully autonomous multi-input single-inductor multi-output energy-harvesting and power-management platform with 1.2×105 dynamic range, integrated MPPT, and multi-modal cold start-up," in *Proc. IEEE Int. Solid-State Circuits Conf.*, 2022, vol. 65, pp. 1–3.

[9] Z. Chen, M.-K. Law, P.-I. Mak, W.-H. Ki, and R. P. Martins, "Fully integrated inductor-less flipping-capacitor rectifier for piezoelectric energy harvesting," *IEEE J. Solid-State Circuits*, vol. 52, no. 12, pp. 3168–3180, Dec. 2017.

[10] X. Yue and S. Du, "Voltage flip efficiency optimization of SSHC rectifiers for piezoelectric energy harvesting," in *Proc. IEEE Int. Symp. Circuits Syst.*, 2021, pp. 1–5.

[11] Z. Li et al., "Piezoelectric energy harvesting interface using self-bias flip rectifier and switched-PEH DC–DC for MPPT," *IEEE J. Solid-State Circuits*, vol. 59, no. 7, pp. 2248–2259, Jul. 2024, doi: 10.1109/JSSC.2023.3341865.

[12] Z. Chen, M.-K. Law, P.-I. Mak, X. Zeng, and R. P. Martins, "Piezoelectric energy-harvesting interface using split-phase flipping-capacitor rectifier with capacitor reuse for input power adaptation," *IEEE J. Solid-State Circuits*, vol. 55, no. 8, pp. 2106–2117, Aug. 2020.

[13] J. Wang, Z. Chen, Z. Li, J. Jiang, J. Liang, and X. Zeng, "Piezoelectric energy harvesters: An overview on design strategies and topologies," *IEEE Trans. Circuits Syst. II, Exp. Briefs*, vol. 69, no. 7,pp. 3057–3063, Jul. 2022.

[14] S. Du and A. A. Seshia, "A fully integrated split-electrode synchronized-switch-harvesting-on-capacitors (SE-SSHC) rectifier for piezoelectric energy harvesting with between 358% and 821% power-extraction enhancement," in *Proc. IEEE Int. Solid-State Circuits Conf.*, 2018, pp. 152–154.

[15] S. Du, Y. Jia, C. Zhao, G. A. J. Amaratunga, and A. A. Seshia, "A fully integrated split-electrode SSHC rectifier for piezoelectric energy harvesting," *IEEE J. Solid State Circuits*, vol. 54, no. 6, pp. 1733–1743, Jun. 2019.

[16] M. Meng, "27.4 Multi-beam shared-inductor reconfigurable voltage/SECE-mode piezoelectric energy harvesting of multi-axial human motion," in *Proc. IEEE Int. Solid-State Circuits Conf.*, 2019, pp. 426–428.

[17] J. Wang et al., "Enhancing efficiency in piezoelectric energy harvesting: Collaborative-flip synchronized switch harvesting on capacitors rectifier and multioutput DC-DC converters utilizing shared capacitors," *IEEE J. Solid-State Circuits*, vol. 60, no. 4, pp. 1474–1485, Apr. 2025.

[18] Y. Sun, N. H. Hieu, C.-J. Jeong, and S.-G. Lee, "An integrated high-performance active rectifier for piezoelectric vibration energy harvesting systems," *IEEE Trans. Power Electron.*, vol. 27, no. 2, pp. 623–627, Feb. 2012.

[19] X.-D. Do, H.-H. Nguyen, S.-K. Han, D. S. Ha, and S.-G. Lee, "A self-powered high-efficiency rectifier with automatic resetting of transducer capacitance in piezoelectric energy harvesting systems," *IEEE Trans. Very Large Scale Integr. Syst.*, vol. 23, no. 3, pp. 444–453, Mar. 2015.

[20] L. Wu, X.-D. Do, S.-G. Lee, and D. S. Ha, "A self-powered and optimal SSHI circuit integrated with an active rectifier for piezoelectric energy harvesting," *IEEE Trans. Circuits Syst. I, Reg. Papers*, vol. 64, no. 3, pp. 537–549, Mar. 2017.